Plasma Sources
Science and
Technology

Modeling Filamentary Transitions in an ArF Excimer Laser

To cite this article before publication: Luying Bai *et al* 2025 *Plasma Sources Sci. Technol.* in press https://doi.org/10.1088/1361-6595/ae1385

Modeling Filamentary Transitions in an ArF Excimer Laser

Luying Bai[1], Xiaochi Ma[1], Yifei Zhu[1], Yun Wu[1]

[1] National Key Lab of Aerospace Power System and Plasma Technology, Xi'an Jiaotong University, Xi'an, 710049, People's Republic of China

E-mail: yifei.zhu.plasma@gmail.com

Abstract.

Filament formation in excimer laser discharge chambers often leads to premature termination of optical pulses, serving as a key factor affecting laser spatial homogeneity and energy stability. This study develops a 0–2D hybrid discharge model for ArF laser discharge chambers to simulate non–uniform glow–filament discharge transitions. The localized halogen depletion near hotspots during filament growth are observed, with discharge non–uniformity evolution qualitatively consistent with experimental observations. We make semi-quantitative analysis about the impact of filaments on glow discharge energy and total ArF^* production, finding that the ArF^* yield per unit energy in filament regions was found to be only 10%–12% of that in glow regions. By adjusting magnetic pulse compression (MPC) excitation circuit parameters, the energy allocation between filaments and glow discharge are improved, reducing laser energy drop caused by filaments.

Keywords: ArF excimer laser, numerical modelling, filamentary transition, plasma

1. Introduction

The 193 nm ArF excimer laser, characterized by its short wavelength (193 nm) and high intrinsic efficiency, are widely used in refractive surgery [1, 2], micro–nano fabrication [3–5], and surface ablation [6, 7]. Additionally, it holds distinct advantages as a prospective driver for frontier strong–field physics studies like inertial confinement fusion (ICF) [8, 9]. Recent studies by NRL (the U.S. Naval Research Laboratory) researchers have further explored the feasibility of ArF lasers for ICF applications, achieving a ArF laser energy of 200 J [10].

In most applications of ArF lasers, long and stable laser pulses are essential. However, in high-voltage conditions, the formation of filaments (manifested as narrow channels with high current or electron density) will disrupt the optical homogeneity needed for laser operation [11], and ultimately cause the laser pulse to terminate earlier than the discharge pulse [12, 13]. Additionally, filament formation causes severe discharge inhomogeneities, which often leads to perturbations in gas density [14] or

in vapourization of the electrode material [15]. Both of these events can lower the repetition rate performance of the laser, limiting its operational efficiency. Consequently, researchers are interested in the mechanisms behind filament generation and suppression.

The mainstream theory attributes the formation of filaments in rare gas halide lasers to cathode instability. Treshchalov et al. [16] reported in their study that the cathode hot spots, when airflow cooling is absent, will induce the discharge channel contracting into filaments. Belasri et al. [17] and Akashi et al. [18] studied the evolution of the cathode sheath in XeCl and ArF Lasers respectively, suggesting the formation of instabilities in the cathode region is closely related to filamentation.

Another hypothesis about the mechanism of filament formation is the non–uniform distribution of the halogen donor or its depletion. Coutts et al. [19] considered halogen donor depletion during the discharge pulse as the principal cause of discharge collapse and the termination of lasing. Kushner [20] predicted that operating point instabilities, which arise from the non–uniform distribution of halogen density or preionization electron density, are the origin for the formation of filaments. In most cases, the effects of these two mechanisms are combined and reinforce each other.

For the filament formation, there are studies indicate that the filaments originate from their own hotspots within the homogeneous plasma initially, rather than forming as thin channels directly connecting the electrodes [21]. After formation, the filaments will "consume" the uniform glow discharge [22], resulting in energy redistribution between filaments and uniform glow discharges [23], and ultimately terminate the laser pulse. Therefore, filament formation occurs later than the uniform glow discharge, with temporal overlap between this two discharge modes. Additionally, discharge inhomogeneities often occur across multiple dimensions. Taylor's research demonstrates that as a result of the filamentation, the "glow" discharge collapses both transverse to and in the electric field direction [22].

From the studies above, it can be observed that filaments and the glow discharge are spatially interconnected and coexist during the discharge. Furthermore, since both are powered by the same electrode, they will compete for power, mutually influencing each other. Therefore, to analyze the impact of filamentary transitions on the overall discharge characteristics, models must account for both discharge modes.

For 0–1D models, Kushner [20] developed a 1D combined microarc–bulk model for KrF lasers under $Kr/He/F_2$ gas mixtures. This model assumes a uniform distribution of components along the vertical direction between the electrodes, treating micro arcs as randomly dispersed across the discharge volume. In this study, Kushner proposes the operating point instability (OPI) theory, attributing the formation of filaments to uneven halogen density or preionization electron density.

Demyanov and Krause [24, 25] developed a 1D filament-volume hybrid discharge model based on parallel–resistor model (PRM) [26] for excimer lasers, which simplifies the treatment of filaments while accounting for the real electrode profiles. This model was used to study the redistribution of current between two discharge modes and discharge instabilities caused by halogen depletion.

These studies have explored the impact of filaments on circuit parameters and the reaction kinetics of filaments. However, current research models that consider both filaments and glow discharges are confined to low–dimensional, making it difficult to reflect the complex chamber structure and self–consistent preionization process. Moreover, the treatment of filaments is highly simplified, neglecting the propagation and contraction dynamics during filamentation.

Therefore, some researchers try to study the self-consistent formation progress of filaments, or pre–ionization process under the detailed chamber structure through 2D model. Bychkov et al. [27, 28] ignored the transverse distribution of filaments along electrodes and assumed the cathode hotspot as an elongated ridge in the transverse direction. This allowed them to study discharge non–uniformity in a 2D model for the first time. Akashi et al. [29, 30] used an axisymmetric 2D plasma fluid model to analyze how cathode hotspots affect discharge uniformity, but their simplification of electrode geometry was significant, making the model closer to an abstract idealization for qualitative discussion. The only 2D excimer laser model considering complex discharge chamber structures is Xiong and Mark J Kushner's [31] work about ArF lasers, which focused solely on the impact of UV preionization produced by the corona–bar discharge on the main gap discharge under uniform glow discharge conditions.

However, these models either consider only single–dimensional non–uniformity because a 2D cross-section inherently assumes a uniform morphology in the third dimension, or they focus solely on uniform discharges, without capturing the interaction between the two discharge modes.

In summary, although considerable research has been conducted on discharge instability in excimer lasers, no analysis simultaneously considers the accurate geometry (2D or higher) and the interaction between filament and glow discharge. The formation mechanism of filaments and their impact on discharge non–uniformity have not been deeply and quantitatively analyzed. Therefore, this study: (1) innovatively established a 0D–2D hybrid model that considers both glow and filament discharges, combined with a self–consistent external MPC circuit, and artificially constructed electrode hotspots to analyze the evolution and formation mechanisms of filaments in the laser; (2) semi-quantitatively analyzed how filament formation affects glow discharge power and ArF^* yield, based on the tight coupling between filamentary and glow discharges; (3) studied the influence of magnetic pulse compression circuit on filamentary discharge and offered suggestions for suppressing filament formation by adjusting the circuit parameters.

2. Numerical Model Description

This study models the glow–to–filament transition in excimer laser discharge chambers. Since filamentary and glow discharges differ in characteristics (e.g., discharge morphology and formation times) yet coexist and interact with each other, we split the discharge into two parts: filamentary discharge (analyzed using a 2D model) and uniform glow discharge (analyzed using a 0D model). Artificial electrode hot spots

are introduced into the 2D filament model to reflect the non–uniformity both between filament–glow and within the filament. The two discharge modes influence each other through an independent external circuit module.

2.1. 2D fluid model for the filament discharge

For the filamentary discharge region, a 2D model is employed due to its high spatial non–uniformity. This study uses the 2D plasma–fluid code *PASSKEy* (Parallel Streamer Solver with KinEtics) to simulate nanosecond discharges in ArF excimer lasers. Previous studies [32, 33] have demonstrated that the local mean energy approximation (LMEA) provides higher accuracy in electron density compared to the local field approximation and is more suitable for atmospheric–pressure simulations. Therefore, the LMEA is adopted in this model, with related code validations provided in published works [34,35]. The main governing equations used in the model are presented below:

The species drift–diffusion equation is:

$$\frac{\partial n_i}{\partial t} + \nabla \cdot \mathbf{\Gamma}_i = S_i + S_{ph},\ i = 1, 2, \ldots, N_{total} \tag{1}$$

where n_i is the number density of specie i, t is time, S_i is the reaction source term of specie i, S_{ph} is the photoionization term, $\mathbf{\Gamma}_i$ is the plasma component flux caused by convective and diffusion, and its expression is:

$$\mathbf{\Gamma}_i = \left(q_i / |q_i|\right) \mu_i n_i \boldsymbol{E} - D_i \nabla n_i, i = 1, 2, \ldots, N_{charge} \tag{2}$$

where q_i is the charge number of specie i, D_i is the diffusion coefficient and μ_i is the mobility of specie i, respectively. $\boldsymbol{E}$ is the electric field. The electron diffusion coefficient and electron mobility are determined by the mean electron energy in LMEA and calculated by BOLSIG+ [36]. The mobility of ions is calculated using the MOBION [37] program, and the diffusion rate is determined by the Einstein relationship:

$$D = \mu \left(k_b T / e\right), \quad k_b = 1.38 \times 10^{-23}\ J/K, e = 1.602 \times 10^{-19}\ C. \tag{3}$$

The electron energy conservation equation is:

$$\frac{\partial n_e \epsilon_m}{\partial t} + \nabla \cdot \mathbf{\Gamma}_\epsilon = -\left|q_e\right| \cdot \mathbf{\Gamma}_e \cdot \boldsymbol{E} - P\left(\epsilon_m\right) \tag{4}$$

where n_e is the electron density, ϵ_m is the mean electron energy, $\mathbf{\Gamma}_\epsilon$ and $\mathbf{\Gamma}_e$ are the fluxes of electron energy and electron, respectively, and $P\left(\epsilon_m\right)$ is the power by collisions. The expression for $\mathbf{\Gamma}_\epsilon$ is:

$$\mathbf{\Gamma}_\epsilon = -\mu_\epsilon n_e \epsilon_m \boldsymbol{E} - D_\epsilon \nabla \left(n_e \epsilon_m\right) \tag{5}$$

where μ_ϵ is the electron energy mobility, and D_ϵ is the electron energy diffusion coefficient.

The electric field is determined by solving the Poisson's equation coupled with space charge:

$$\nabla\left(\varepsilon_0\varepsilon_r(-\nabla\Phi)\right) = -\rho - \rho_c \tag{6}$$

$$\boldsymbol{E} = -\nabla\Phi \tag{7}$$

$$\rho = \sum_{i=1}^{N_{ch}} n_i q_i \tag{8}$$

$$\frac{\partial\rho_c}{\partial t} = \sum_{i=1}^{N_{ch}} q_i(-\nabla\cdot\boldsymbol{\Gamma}_i) \tag{9}$$

where ε_0 is the vacuum permittivity, ε_r is the relative permittivity, Φ is the potential, $\boldsymbol{E}$ is the electric field, ρ is the space charge, and ρ_c is the surface charge determined by the flux of ions $\boldsymbol{\Gamma}_{ion}$ at the interfaces between the plasma and the dielectric. The curvature of the electrode and the electric field enhancement are extremely important for pulsed, high–pressure discharges. To avoid the serration shape caused by cartesian mesh generation, the immersed boundary method [38] was used at the boundaries in Poisson's equation. The detailed setup and validation of the 2D fluid model for the ArF excimer laser discharge chamber have been fully described in our previous paper [39] and will not be repeated here.

The partial 2D section diagram of ArF excimer lasers is shown in Figure 1(a), with dimensions of 31 mm x 31 mm. The diagram includes the cathode (copper, colored in red), anode (copper, colored in blue), dielectric (alumina ceramic, colored in yellow, with the relative permittivity ε_r=8), and the plasma region (colored in white). Figure 1(a) only contains the components that are relevant to the computational results, while neglecting those that are not important. It is worth mentioning that the corona bar is included in the computational domain, as it plays a significant role in providing photo–generated electrons for the main gap. The numerical model employs the structured adaptive mesh refinement in a 2D Cartesian coordinate system. The mesh is initialized based on the geometry shape shown in Figure 1(b). The criteria for adaptive mesh refinement is based on the electron density.

The simplified ArF reaction scheme employed in this study considers four basic gas components: Ar, F_2, Ne, and Xe. The simulation is conducted under a pressure of 3.4 atm, with an initial electron density set to a low value of $n_e = 10^6$ m^{-3} [40]. There are 44 plasma reactions involving 20 plasma species, including electrons, excited state particles, positive ions, and negative ions. Specific species are shown in Table 1. The complete plasma chemistry, simplifying strategy, and stoichiometric ratio can be seen in our previous paper [39]. The model's reaction scheme remains consistent throughout the work, including the 2D model in this section and the 0D model in the next section.

In addition, to introduce the unstable disturbances that induce filament formation, a hundred–micrometer–scale deformation with high secondary electron emission coefficients was added to both the cathode and anode, aiming to replicate the local

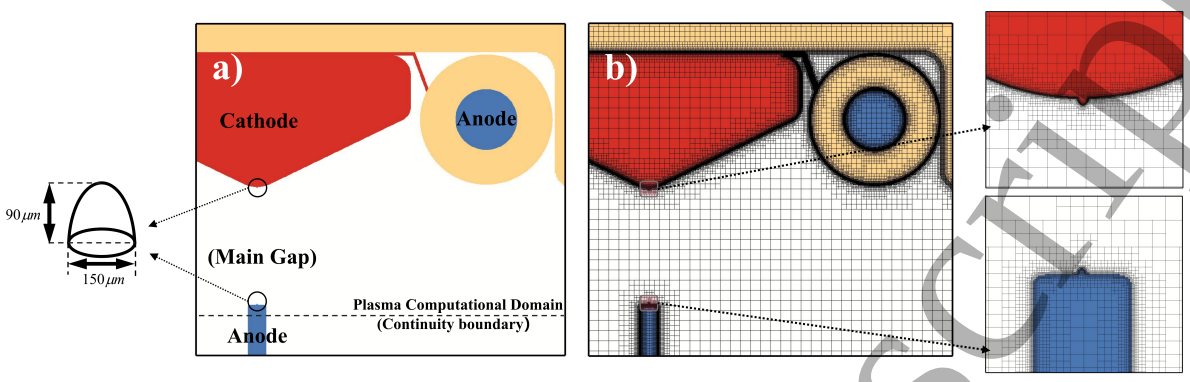

Figure 1: (a) The partial 2D section diagram of ArF excimer lasers with electrode protrusion. (b) the initial meshes with geometric refinement.

Table 1. List of plasma species

Species	Name
Neutral Species	Ar, F_2, Ne, Xe, F
Ar Excited Species	Ar^* (sum of 4s), Ar^{**} (sum of 4p), Ar_2^*
Ne Excited Species	Ne^* (sum of 3s), Ne_2^*
Dimer Species	ArF^*, Ar_2F^*
Positive Charged Species	Ar^+, F_2^+, Ne^+, Xe^+, Ar_2^+, Ne_2^+
Negative Charged Species	F^-, e^-

electric field disturbances caused by ablation and chemical corrosion in experiments. The selection of the deformation size is based on research by Dreiskemper and Guo on typical sizes of hot spots and corrosion pits on copper alloy electrodes in excimer laser [21,41–43]. For the deformation shape, we adopted a simplified but representative ellipsoidal protrusion geometry, which can effectively simulate the local electric field enhancement effect of a hotspot and induce a glow-to-filament transition. This simplification allowed us to focus more on the influence of the electrode surface microstructure on filamentation behavior, rather than becoming entangled in complex and difficult-to-quantify shape details. The specific size and schematic structure of the adopted deformation are shown in Figure 1.

2.2. Global model for the glow discharge

To enhance computational efficiency, the discharge in the uniform glow region is simplified to a 0D dynamical model. To validate this simplification, a 2D fluid model was first used to simulate the glow discharge. It was found that, under the pre–ionization produced by the UV photoionization model in this paper, the spatial distribution of electron density during the glow discharge is relatively uniform. Under this study's simulation objective and conditions, the process can be simplified to a 0D model. For

a detailed discussion of the impact of photoionization on the discharge in ArF laser chambers, please refer to our previous paper. [39].

In the 0D model, the reaction source term S_i reflects the changes caused by plasma reactions. S_i using a set of ODE equations to describe:

$$\frac{dn_i}{dt} = S_i = \sum_{j=1}^{j_{max}} Q_{ij},\ j = 1, 2, 3, \ldots, j_{max},\ i = 1, 2, 3, \ldots, N_{total} \tag{10}$$

where j is the number of the reaction, i is the number of species, and Q_{ij} is the source term of species i from reaction j.

The reduced electric field in the 0D model is given by equation $E = U_{ext}/(d_{gap} \cdot N)$, where U_{ext}, d_{gap} and N denote the electrode voltage, electrode separation, and neutral gas density, respectively. The calculation of current relies on the discharge cross-sectional dimensions obtained from the 2D glow simulation, with specific setting basis detailed in Section 2.3. Tests show that with an initial electron density of $n_{e0} = 3 \times 10^{15}$ m^{-3}, the electrode voltage curve obtained from the 0D simulation (solid line in Figure 2) almost coincides with the results from the 2D simulation. Additionally, the time evolution of electron density (dashed lines in Figure 2, with the 2D model's density extracted from the midpoint of the electrode's central axis) shows good agreement between the 0D and 2D models during the main discharge stage and breakdown moment, except for minor deviations in the initial electrode charging stage and afterglow stage. Since electron density is low during these phases and has negligible impact on electrode voltage, the simplified 0D model provides acceptable accuracy for our hybrid model.

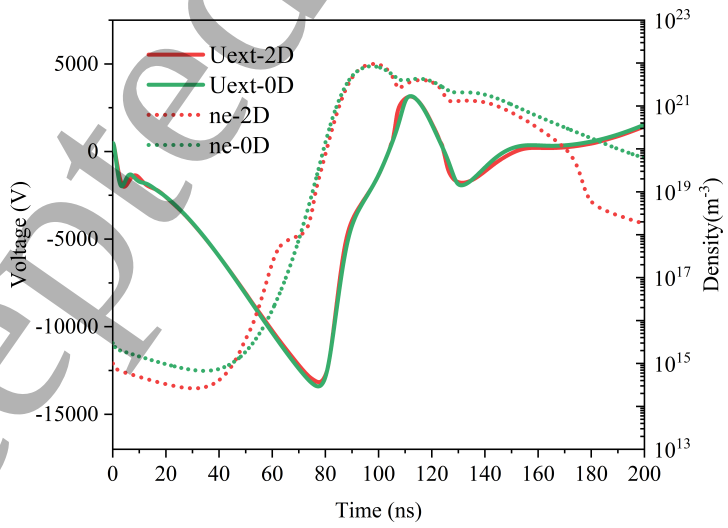

Figure 2: The temporal evolution of electrode voltage and electron density in glow discharge, as calculated by 0D and 2D models.

2.3. External circuit module and coupling strategy

The 2D filament and 0D glow models are integrated with the external circuit module and solved together. The simplified external circuit for the excimer laser and its coupling strategy with the plasma module are shown in Figure 3. Here, the MPC–circuits are simplified as a circuit consisting of four components: L_1, L_2, C_1, and C_2, where C_1 is the primary storage capacitor and C_2 is the tunable peaking capacitor; L_1 is a combination of the magnetic switch inductor and the pre–ionization stray inductor, and L_2 is a collection of discharge stray inductors. Capacitor C_1 has an initial voltage and is assumed to be connected to the circuit at the start of the simulation. At the same time, C_2 will be rapidly charged by C_1, generating hundred–nanosecond–scale voltage pulses.

In the circuit module, the plasma is equivalent to a current source, with its current value being the sum of the currents obtained from the filament and glow models. The external circuit module calculates the electrode voltage by solving an ODE system based on Kirchhoff's law, then feeds the results into the 0D/2D models to update the reduced electric field in the next time step.

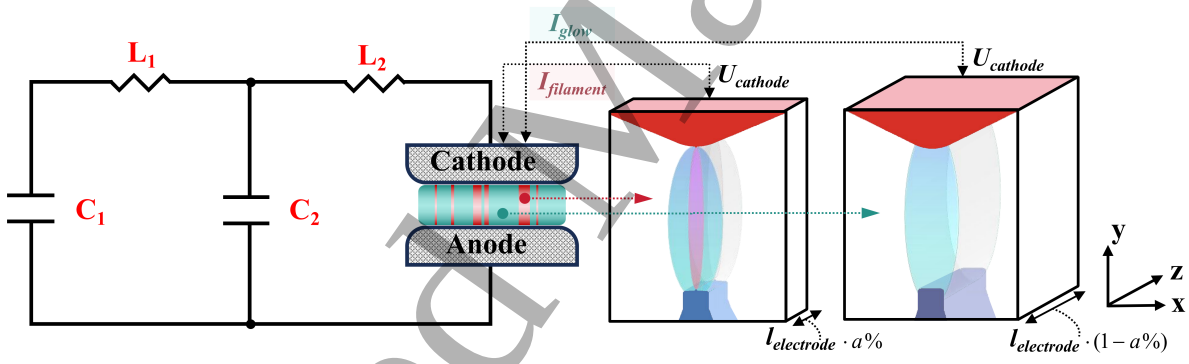

Figure 3: The coupling strategy between the 2D filament and 0D glow models with the external circuit modules.

The numerical model assumes filament and glow regions occupy different proportions along the z–axis. Parameter $\alpha\%$ represents the z–axis coverage ratio of filamentary areas, estimated using methods from Ref. [24] based on experimental filament counts and simulated radius: The filament quantity adopts averaged values from five repeated experiments under identical conditions, while radius obtained from 2D simulations with electrode disturbances under the experimental voltage. This value is estimated to be 2% for our configuration. Unless specified in Section 3.2, which discusses the effects of filament proportion, all simulations default to this value. Correspondingly, the fraction of the glow region is $(1 - \alpha\%)$. The z–axis lengths of filaments and glow discharge are $l_{electrode} \cdot \alpha\%$ and $l_{electrode} \cdot (1 - \alpha\%)$, respectively, where $l_{electrode}$ denotes the total longitudinal electrode length based on experimental dimensions.

The current of the 2D filament model is calculated by Eq. 11:

$$I = \int_{electrode} (\sum_{i=1}^{N_{total}} q_i \varphi_i + \frac{d(\varepsilon \boldsymbol{E})}{dt}) \cdot \hat{n} dS,\ i = 1, 2, 3, \ldots, N_{total} \tag{11}$$

where i is the number of species, q_i and φ_i represent the charge and flux magnitude of species i at the electrode surface, respectively, ε is the permittivity, $\boldsymbol{E}$ is the electric field at the electrode surface, and $\boldsymbol{n}$ is the unit normal vector at the electrode surface. The 2D model's electrode current can be divided into two parts: the displacement current and the conduction current. The conduction current is obtained by integrating the fluxes of various charged species on the electrode surface, while the displacement current is the integration of the derivative of the potential displacement vector over time on the electrode surface.

The current of the 0D glow model is calculated by Eq. 12:

$$I = \sum_{i=1}^{N_{total}} q_i n_i \mu_i E \cdot S |U_{ext}| / (U_{ext}),\ i = 1, 2, 3, \ldots, N_{total} \tag{12}$$

where the subscript i denotes the number of species, with q_i, n_i, and μ_i representing the charge, density, and mobility of species i, respectively. The electric field is given by $E = U_{ext}/d_{gap}$, and the current cross–sectional area $S = (1 - \alpha\%) \cdot l_{electrode} \cdot w_{plasma}$. The selection of the discharge channel width, w_{plasma}, is based on the plasma dimensions calculated from 2D glow discharge simulations: in the 2D simulations, the width of the region enclosed by the isodensity line where the electron density decays to 1/e of the maximum value at the central axis is defined as the discharge channel width, w_{plasma}. This value is maintained at approximately 2 mm during the main discharge phase after breakdown. Our previous experimental and simulation results indicate that the displacement current magnitude under our experimental conditions is negligible compared to the conduction current. Consequently, only the conduction current is considered in the 0D current calculation.

Figure 4 shows the circuit outputs obtained from the 0–2D hybrid model and experiment. The simulated and experimentally measured C1 and C2 voltage curves match well in the drop timing, drop slope, and oscillation peak, indicating that the calculated breakdown voltage and electron density evolution are highly accurate.

It should be emphasized that the actual chamber discharge process is highly complex. The formation of hotspots typically results from a combination of factors, including gas/solid impurity diffusion and sputtering, physical ablation, and chemical erosion. Moreover, the associated electrode erosion is likely to be dynamic. A fully self-consistent description of all these processes would require complete 3D simulations, necessitating significant computational resources and excessively long iteration cycles. Our goal is therefore not to replicate the real discharge process perfectly but to establish a numerical model that can explore and explain the laser discharge transition and its effects. To achieve this, the present model employs a simplified treatment of the hotspot formation mechanism and utilizes several simplifications, such as zonal discharge computation and model order reduction. As a result, the findings are primarily focused

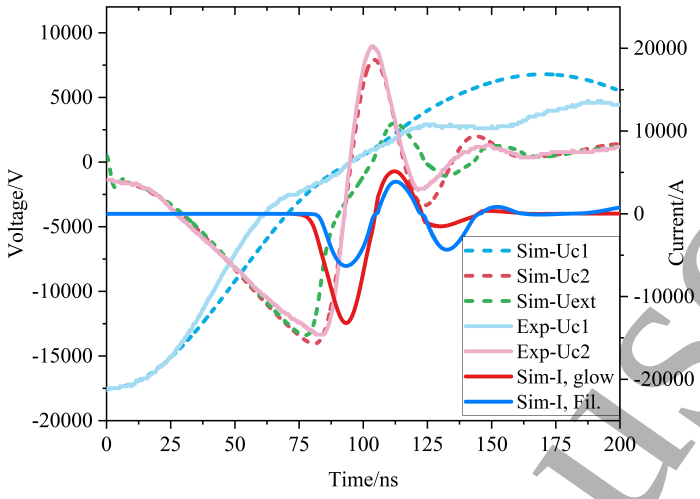

Figure 4: Comparison of circuit outputs obtained from the simulation and experiment, with I_{glow} and I_{Fil}. (currents in glow and filament regions), and U_{C1}, U_{C2}, U_{ext} (voltages across capacitors C_1, C_2, and the electrode).

on providing qualitative insights into physical mechanisms and semi-quantitative trend analysis, instead of highly precise quantitative predictions.

3. Results and discussion

3.1. Filament Evolution and Formation Mechanisms

The evolution of discharges both with and without filamentary transitions are illustrated in Figure 5 (a) and (b), and the experimental comparisons from ICCD images is shown in Figure 5 (c). The spatial relationship between the 2D simulation section, ICCD camera imaging viewpoint, and the discharge chamber is shown in Figure 6. The camera captured images from the side of the discharge chamber, with a pulse trigger controlling the camera's triggering time and adjusting the relative timing between the camera shutter and the experimental voltage. The gate width of the ICCD camera was set to 5 ns. The numerical models using the same initial circuit settings and gas mixture conditions as experiment. It should be noted that the observation directions for experimental imaging and numerical simulation are perpendicular to each other. Therefore, in this section, we only compares discharge uniformity's time–evolution characteristics rather than the specific discharge morphology.

We first employed a 2D model to study the evolution of pure glow discharge (Figure 5(a)). Due to sufficient preionized electrons generated before breakdown, the electron density distribution in the discharge channel remains uniform with low gradients. The discharge maintains glow mode until termination with voltage decay, which contradicts experimental observations. In reality, ICCD images reveal distinct

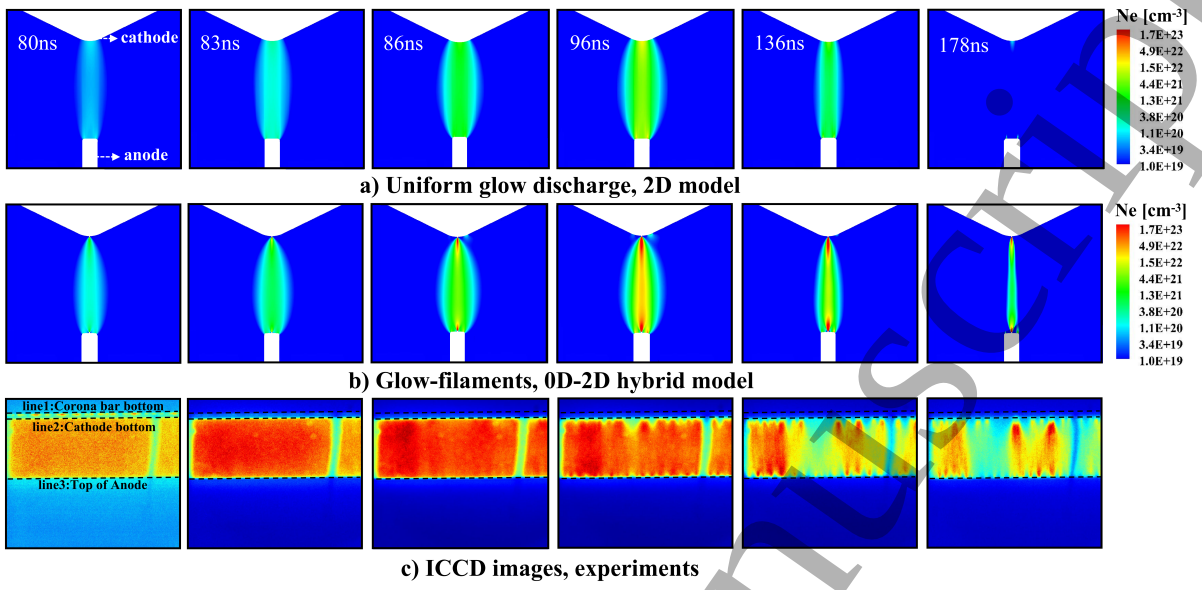

Figure 5: (a-b) The evolution of channel electron density with and without filamentary transitions. (c) The corresponding experimental ICCD images at specific moments.

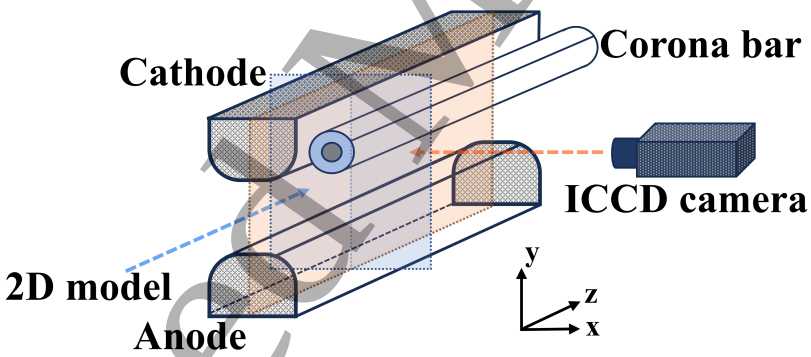

Figure 6: The spatial relationship between the 2D simulation section, ICCD camera shooting direction, and discharge chamber.

hotspots at both the cathode and anode, followed by discharge channel contraction into filaments along these hotspots. This indicates that pure 2D model based on uniform glow discharge assumptions cannot accurately reflect actual physical processes. Thus, we developed a hybrid model combining 2D filamentary and 0D glow discharge to investigate inhomogeneous discharge evolution. Numerical results show that although pure glow discharge and glow–filament hybrid discharge share similar breakdown times and electron density peak times, they exhibit significant differences in discharge morphology and species densities.

The numerical results from the hybrid model are shown in Figure 5(b), which demonstrates the non–uniformity evolution of filament along the x and y directions.

Additionally, to compare the z–direction non–uniformity with experiments, the time evolution of electron density from the 2D filament model and 0D glow model and their ratio are plotted Figure 7, with this ratio serving as a simplified indicator of discharge non–uniformity along the z–direction. In the 2D model, the electron density of the filament is extracted from the midpoint of the electrode protrusion connection line.

Based on the discharge evolution obtained from the simulation (Figure 5(b)) and experiment (Figure 5(c)), it can be concluded properly that the non–uniform discharge induced by hot spots undergoes three stages: glow discharge formation and intensification (before 83 ns), non–uniformity development (83 ns–95 ns), and filaments contraction (after 95 ns).

During the glow discharge formation and intensification stages (before 83 ns), the electrode voltage rises to peak value, and then breakdown happens under a relatively uniform UV pre–ionization. Both simulation and experiment appear as a glow discharge mode, continuing to intensify in a uniform morphology after breakdown, with no significant inhomogeneity observed.

During the non–uniform development stage (83–95 ns), the electrode voltage drops rapidly from the breakdown peak. In simulations, small plasma volumes with high electron density ($>10^{23}m^{-3}$) and diameters of 80 μm first appear near the cathode and anode, coinciding with the electrode hot spots appearing time in experiments. These high-density plasma clusters gradually expand outward, eventually connecting the entire channel to form a filament with a diameter of 700 μm. The uniform glow discharge rapidly collapses, characterized by $n_e \geq 10^{22}m^{-3}$ in the filament and $n_e < 10^{22}m^{-3}$ outside the filament. The discharge shows strong x–direction non–uniformity and weak y–direction non–uniformity, while experiments observe emerging y– and z–direction non–uniformity during this stage. Additionally, as seen in Figure 7, the electron density difference between the filament and glow regions sharply increases once hotspots form. After the filament reaches its maximum intensity at 95 ns, the ratio of electron densities between filament and glow achieves its first peak.

During the filament contraction stage (95 ns to discharge end), the electrode voltage enters an oscillatory decaying phase. The average reduced electric field between the electrodes falls below the ionization threshold of the glow region. Thus, as shown in Figure 7, the electron density in the glow discharge basically stops growing during this stage. However, for the filament, due to higher F_2 consumption within it, its ionization threshold becomes lower than the peak voltage during the afterglow oscillations. Therefore, the filament's electron density still shows significant variations within individual oscillation cycles, and the electron density ratio between filament and glow exhibits an oscillatory upward trend. The discharge channel contracts along hot spots, and the difference in electron density between the filament and the glow gradually increases, indicating that the discharge's inhomogeneity along the z–direction further intensifies, which is consistent with the trend observed in the experimental images.

In 2D simulations, the reduced electric field near hotspots can reach 20 Td or higher during breakdown. To simplify the analysis of reaction kinetics during filament

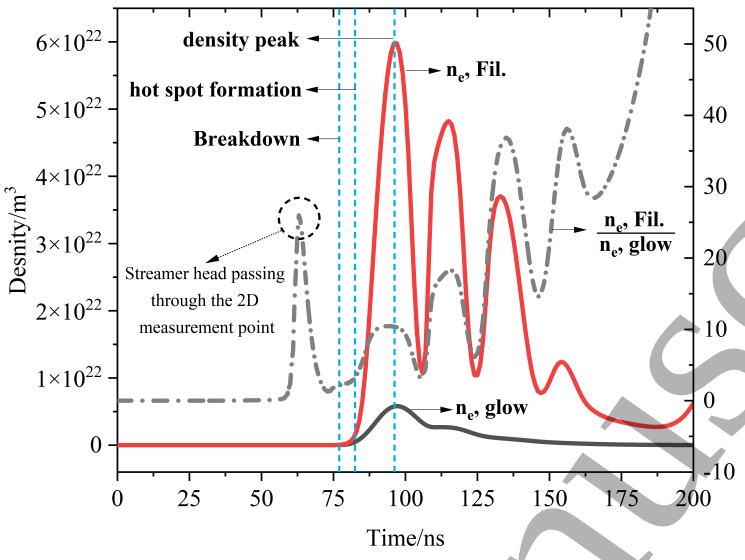

Figure 7: The time evolution of electron density in the filament and glow regions, and their ratio. The solid lines represent the time evolution curves of electron density in the filament and glow regions obtained from simulations, while the dashed lines show their ratio. The filament electron density is extracted from the midpoint of the electrode protrusion connection line.

formation, we conducted a global model study with a fixed reduced electric field of 20 Td. Figure 8(a) shows the temporal evolution of species densities, which are corresponding to three discharge stage based on electron density magnitudes: the glow discharge formation and intensification stage (10^{15}–10^{21}m^{-3}) (stage 1), the non–uniformity development stage (10^{21}–10^{23}m^{-3}) (stage 2), and the filament contraction stage (10^{23}–5×10^{24}m^{-3}) (stage 3). Figure 8(b) and 9 show the proportions of F_2 consumption reactions and electron generation and consumption reactions that contribute more than 1% at different stages. Reactions with a contribution below 3% are displayed without percentage labels.

It can be observed that under the high electric reduced field, the degree of ionization increases. As a result, the dominant reaction for the consumption of F_2 shifts from the harpoon reaction ($Ar^*+F_2 \rightarrow ArF^*+F$), which is also the main reaction generating ArF^* during the glow discharge phase, to the dissociative attachment of F_2 ($F_2+e \rightarrow F^-+F$). This transition reduces the local concentration of F_2, further accelerating the growth rate of electron density and creating a positive feedback loop. Once this process begins, it becomes self–reinforcing, ultimately leading to filament formation.

Simultaneously, the abundant generation of excited-state particles causes the primary electron generation reaction to shift from collisional ionization of Ar to stepwise ionization of Ar. Concurrently, the main electron consumption reaction transitions from dissociative attachment of F_2 to three-body recombination ($e + Ar^+ + Ar \rightarrow Ar^* + Ar$).

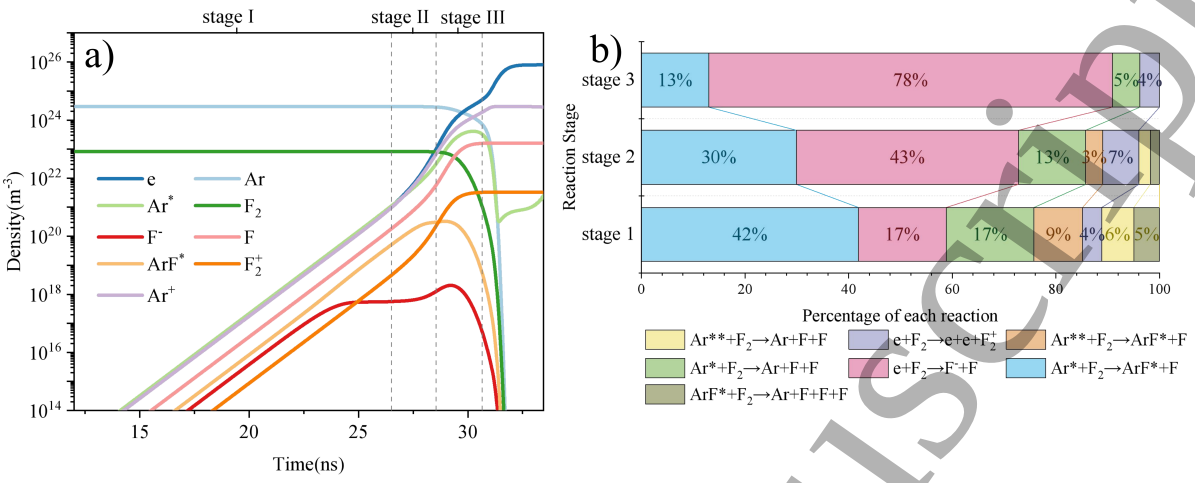

Figure 8: (a) Temporal evolution of component densities at different stages. (b) Dominant F_2 consumption reactions and their contribution percentages at different stages.

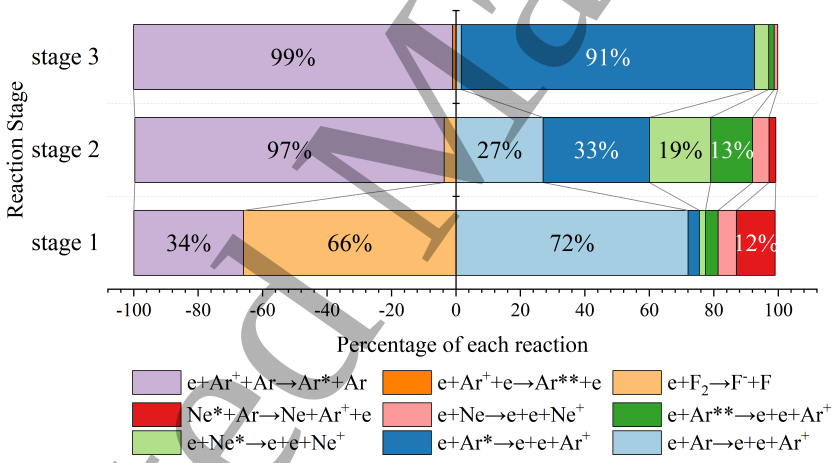

Figure 9: Dominant electron generation/consumption reactions and their contribution percentages at different stages.

3.2. The impact of filamentation on discharge and ArF* *production yield*

Figure 10 shows the simulation results of discharge current and power with and without filamentary transitions. We found that under the first current pulse, there was no significant difference in total current and power between the two conditions. However, when filamentary transitions were taken into account, there was a notable reduction in glow discharge power. This suggests that while the formation of filaments does not considerably alter the total deposition power of the discharge, it does redistribute current between the two discharge modes, leading to a decrease in the power deposited in the uniform glow discharge.

To investigate the impact of filament formation on uniform glow discharge power,

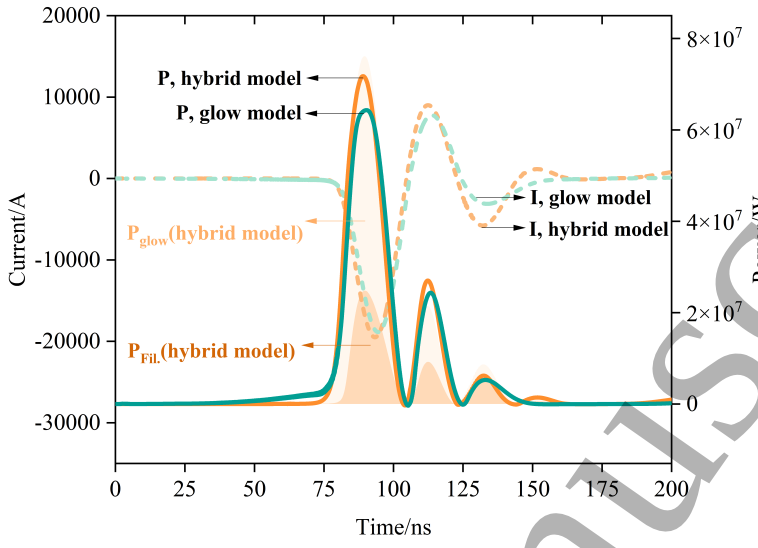

Figure 10: The discharge current and power with and without filamentary transitions, where the light– and dark–colored areas represent the respective part of glow and filamentary discharge power in the hybrid model.

we artificially adjusted the proportion of the filamentary region along the z-axis from 0.25% to 1%. The discharge power absorbed by the filamentary and glow regions and the proportion of filamentary power are plotted in Figure 11. It can be seen that as the proportion of filament along the z-axis increases, its power ratio gradually increases while the glow discharge power declines. After filament formation, the internal electron density can reach (10^{22}–10^{23}m^{-3}), with localized regions near hot spots exceeding 10^{24}m^{-3}. Therefore, even filaments with very low proportions (<1%) can absorb considerable discharge power. When the filament proportion reaches 2%, it will occupy nearly 1/3 of the discharge power, causing the discharge intensity in the remaining glow region to be rapidly weakened. However, as the filament volume ratio increases, its energy growth is not linear but shows a saturation trend.

Additionally, it can be observed that there are three power pulses during the discharge, with the majority of energy release occurring in the first pulse. Since filament growth and formation take time, their power pulses start 8-10 ns later than the glow discharge. From the first to the last pulse, the filament's energy proportion increases from 8%-25% to 25%-60%. When considering the glow and filaments as impedances, they can be treated as being connected in parallel between the electrodes. Due to increased F_2 consumption within the filament during voltage oscillations, its electron density dissipates more slowly compared to the glow region, resulting in lower equivalent impedance values for filaments in the later stages. Consequently, the current is mainly distributed to the filaments during the last pulse.

Figure 12 shows the C_2 voltage curves under different filament proportions. Due to filaments' lower impedance during the afterglow stage, their proportion directly affects

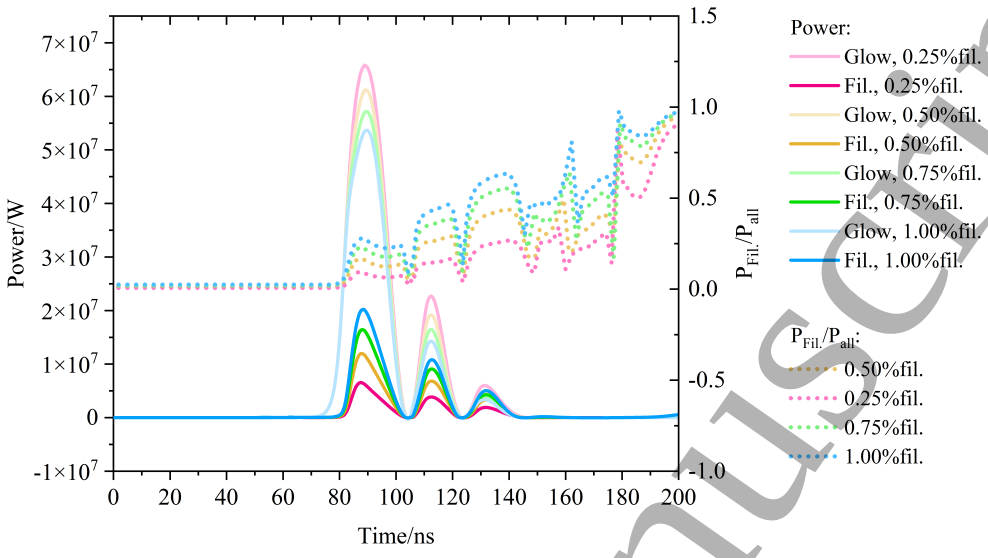

Figure 11: The power absorbed by the filament/glow discharge regions (solid lines) and the filament power percentage of total power (dashed lines) under different z–axial proportions of filament regions.

the damping of LC circuit oscillations, determining the intensity of voltage oscillations. Therefore, the voltage oscillation amplitude in the later stage can serve as an indicator for uniformity evaluation.

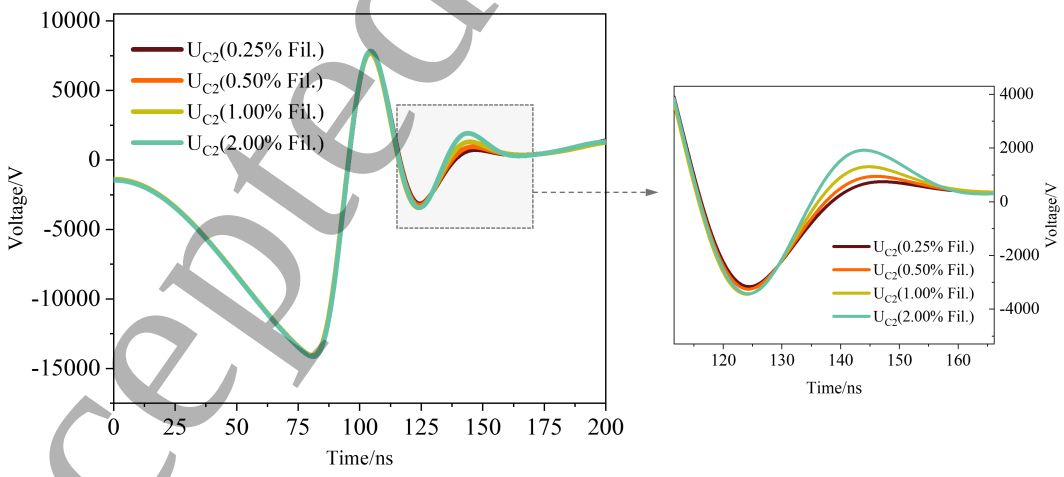

Figure 12: Oscillation amplitude of C_2 voltage during discharge afterglow phase under different z–axial proportions of filament regions.

Filament formation also leads to changes in ArF* generation/consumption pathways. Figure 13 shows the ArF* related reactions contributing over 1% during the glow discharge intensification (stage 1), the non–uniformity development (stage

2), and the filament contraction (stage 3), along with their respective contribution ratios. Figure 14 shows the changes in main ArF*–related reaction pathways before/after filamentation.

The results indicate that after filament formation, the dominant ArF* generation reaction shifts from the harpoon reaction between Ar* and F_2 in the glow phase to three–body recombination reaction of Ar^+ and F^-. This transition arises because the high ionization degree within filament accelerates F_2 dissociation attachment, causing significant F_2 consumption and F^- generation, while a large amount of Ar^+ is produced through stepwise ionization. Meanwhile, the primary ArF* consumption mechanism changes from spontaneous radiation de–excitation to electron–impact de–excitation.

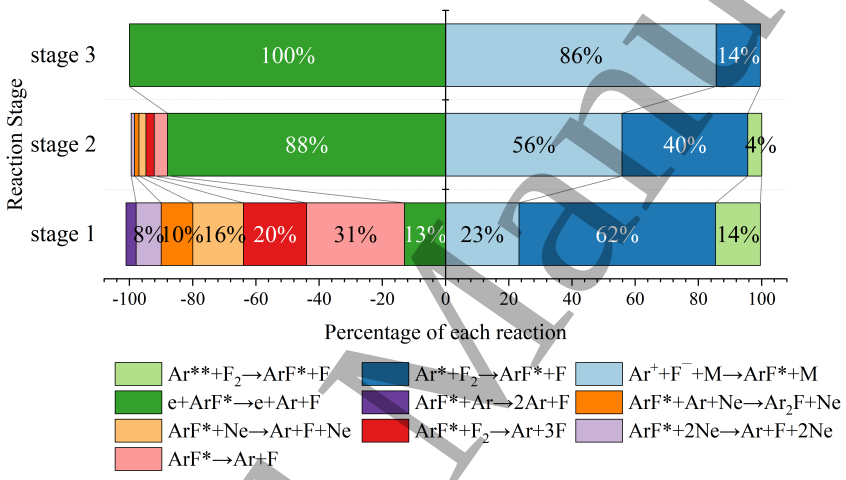

Figure 13: Dominant ArF* generation/consumption reactions and their contributions at different stages. Reactions with a contribution below 3% are displayed without percentage labels.

Due to localized strong fields near hotspots, filamentary discharge shows non–uniformity along the z–axis, making it difficult to quantitatively characterize the impact of filamentation on ArF* yield through simple 0D kinetics model. For further quantitative analysis, densities of key species in the glow region and along the central axis of the filament (at 96 ns when the filament reaches peak intensity) obtained from the hybrid model are compared in Figure 15. The vertical axis Y represents the normalized electrode gap distance, where 0 corresponds to the ground electrode end and 1 to the driven electrode end. The dash–dot lines represent the species densities of glow discharge calculated by the 0D model, while the solid lines represent the species densities within the filament channel calculated by the 2D model.

For the main region of the filament, the components' distribution is relatively uniform, with its electron density about one order of magnitude higher than the glow region. As discussed in Section 3.1, this difference will further increase in later stages. Since F_2 consumption in the central region is relatively light, the high Ar* density caused by the high ionization level within the filament can compensate for F_2 depletion,

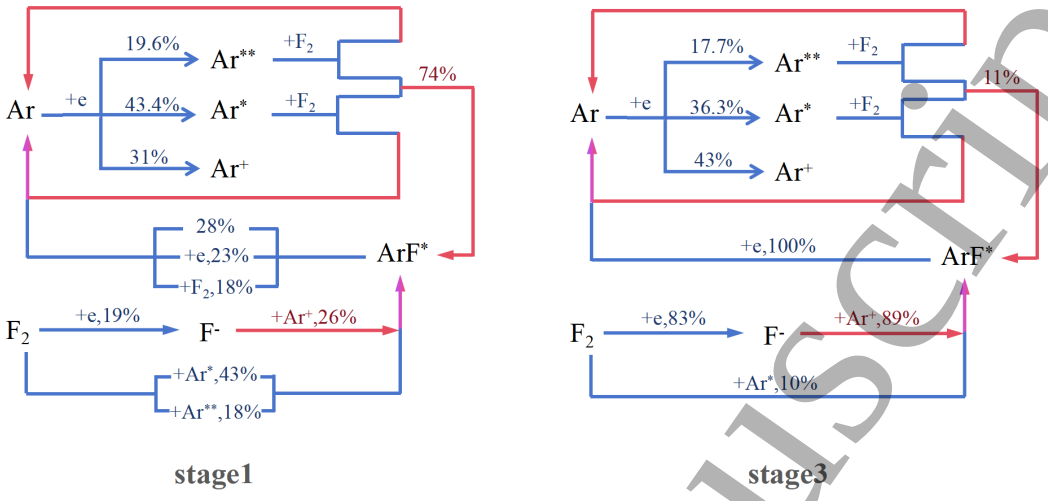

Figure 14: Variations in dominant ArF*–related reaction pathways berfore and after filamentation.

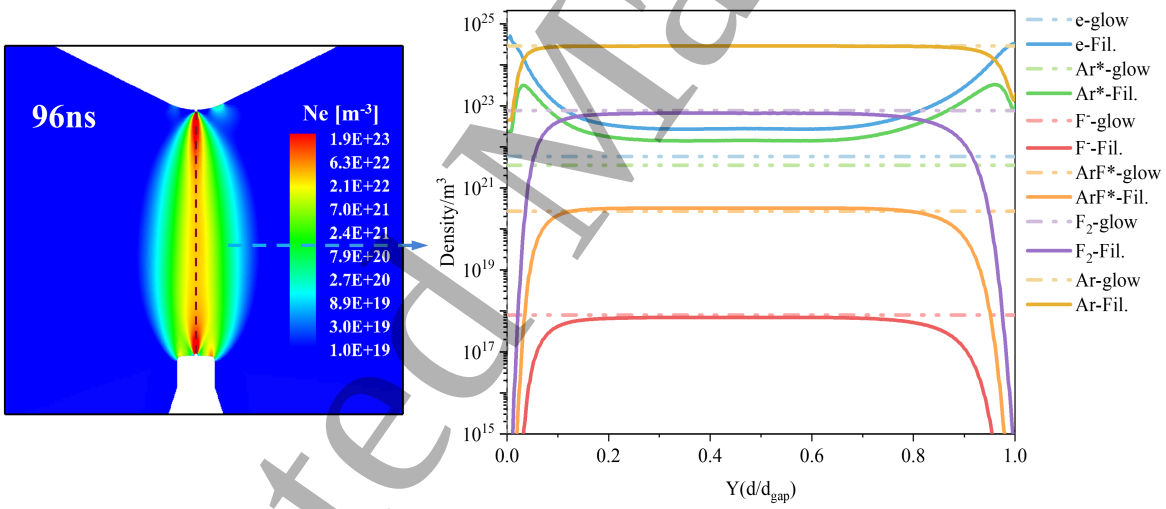

Figure 15: Comparison of the density distribution along the central axis of the electrode for key species between uniform glow/filamentary discharge at 96ns.

ensuring that one of the dominant ArF* generation channels ($Ar^* + F_2 \rightarrow ArF^* + F$) is not excessively weakened. Meanwhile, due to the abundant production of Ar^+ and F^-, another dominant ArF* generation channels ($Ar^+ + F^- + M \rightarrow ArF^* + M$) is enhanced. These combined effects maintain the ArF* density in the main region of filament in the same order of magnitude as in the glow region.

For areas near the electrode, significant F_2 depletion can be observed around hot spots, causing its electron density to be 2–3 orders of magnitude higher than the glow region, while ArF* density becomes 3–4 orders of magnitude lower. Additionally, the density of Ar* first increases and then decreases as it approaches the hot spot, peaking at

about 0.4 mm from the hot spot. This is because the electron density reaches $10^{23}\mathrm{m}^{-3}$ within 1 mm of the hot spot, which leads to strong collisional excitation of Ar. However, as the distance to the hot spot decreases to 0.4 mm, the electron density rises further to $10^{24}\mathrm{m}^{-3}$. At this ionization level, excited states of Ar become heavily consumed through stepwise ionization.

In summary, although the ArF* density in filaments and glow discharges are comparable, their electron densities (especially the region near the cathode, which dominates the current) differ by order of magnitude. This results in the energy deposition density in filaments being 1–2 orders of magnitude higher than in the glow region. Figure 16 shows the absorbed power and ArF* production in the filaments (2% volume fraction) and glow region (98% volume fraction).

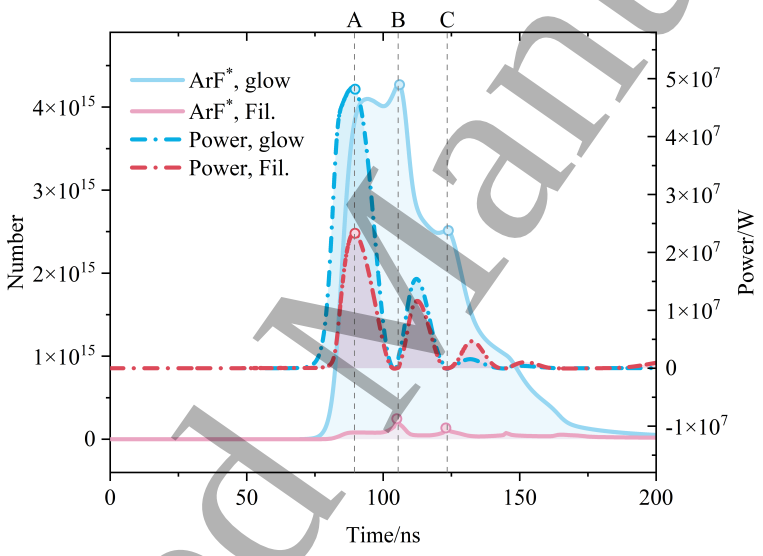

Figure 16: The time evolution curves of absorbed power and ArF* production amount for filament and glow regions with a filament proportion of 2% along the z–axis. The light solid line represents the ArF* production amount, while the dark dashed line represents the absorbed power.

It can be observed that, under the first pulse, the glow region's peak power is only about twice that of filaments (Point A in the figure), but its ArF* production is 15–20 times higher. The ArF* yield per unit energy in the glow region is 8–10 times greater than in the filamentary region. This demonstrates that most power absorbed by filaments is used for ionization, leaving a significantly reduced proportion for ArF* generation. Thus, despite filaments absorbing substantial discharge power, their ArF* yield per unit energy is far lower than in glow discharges. This explains why filament formation leads to decreased laser power and efficiency.

In addition, it can be observed that the density of ArF* shows a small sub–peak each time the power drops to zero (i.e., when the electrode voltage oscillates back to zero, as indicated by points B and C in Figure 16). This is due to the reduction of

the reduced electric field and the accumulation of electron density, which causes the dissociative attachment rate of F_2 to peak near the moment when voltage returns to zero, generating large amounts of F^-. Then these F^- react with the accumulated Ar^+, ultimately leading to sub–peak in ArF^* density.

3.3. Impact of MPC circuit parameters on energy partitioning between filamentary and glow discharge

As discussed in section 3.2, filament's ArF^* production per unit energy is only 10%–12% of that in glow discharge. Therefore, when filamentary transition is unavoidable, we aim to deposit as much energy as possible in the glow discharge. For this target, this section uses simulations to investigate the effects of MPC circuit components on the energy distribution between filament and glow regions, aiming to mitigate the negative impact of filamentation on glow discharge and ArF^* production. This study focuses on two key components influencing circuit response characteristics: the peaking capacitor C_2 and the discharge chamber stray inductance L_2.

The peaking capacitor C_2 mainly affects the steepness of the electrode voltage rising edge. Figure 17 shows the voltage, current, and morphology of filament under different C_2 values.

It can be seen that as C_2 value decreases, the voltage rise slope increases, the current proportion of filaments decreases, and the filament strength becomes weaker. This occurs due to the difference in the initiation time of filaments and glow discharges. Under steep voltage rising edges, overvoltage breakdown leads to higher breakdown voltage, enabling rapid formation and intensification of glow discharges. Energy is released faster into the glow after breakdown, allowing the glow discharge to reach a high level before filaments start developing. Through high current, the glow discharge rapidly releases electrode charge, pulling the voltage down quickly. Therefore, when inhomogeneities around hot spots appear, the voltage has already become lower and will rapidly return to zero. This results in a smaller diameter and lower internal electron density for the filament or even incomplete filament formation.

We define the period from breakdown to the preliminary formation of filaments (I_{Fil}>600 A) as the dominant development stage of glow discharge, and the subsequent period before voltage returning to zero is the dominant development stage of filaments. To show the influence mechanism of C_2 more clearly, we plot the electrode voltage distributions during dominant development stages of glow and filament under different C_2 values and their corresponding power evolution in Figure 18(a-b). It can be observed that larger C_2 values correspond to wider power pulses, longer dominant development durations, and higher average voltages for filaments, consequently resulting in more complete filament development with greater energy consumption.

The discharge stray inductance L_2 primarily governs the energy release rate after breakdown. Figure 19(a-b) present the discharge voltage and current waveform under different L_2 values. It can be observed that at lower L_2, the current exhibits a steeper

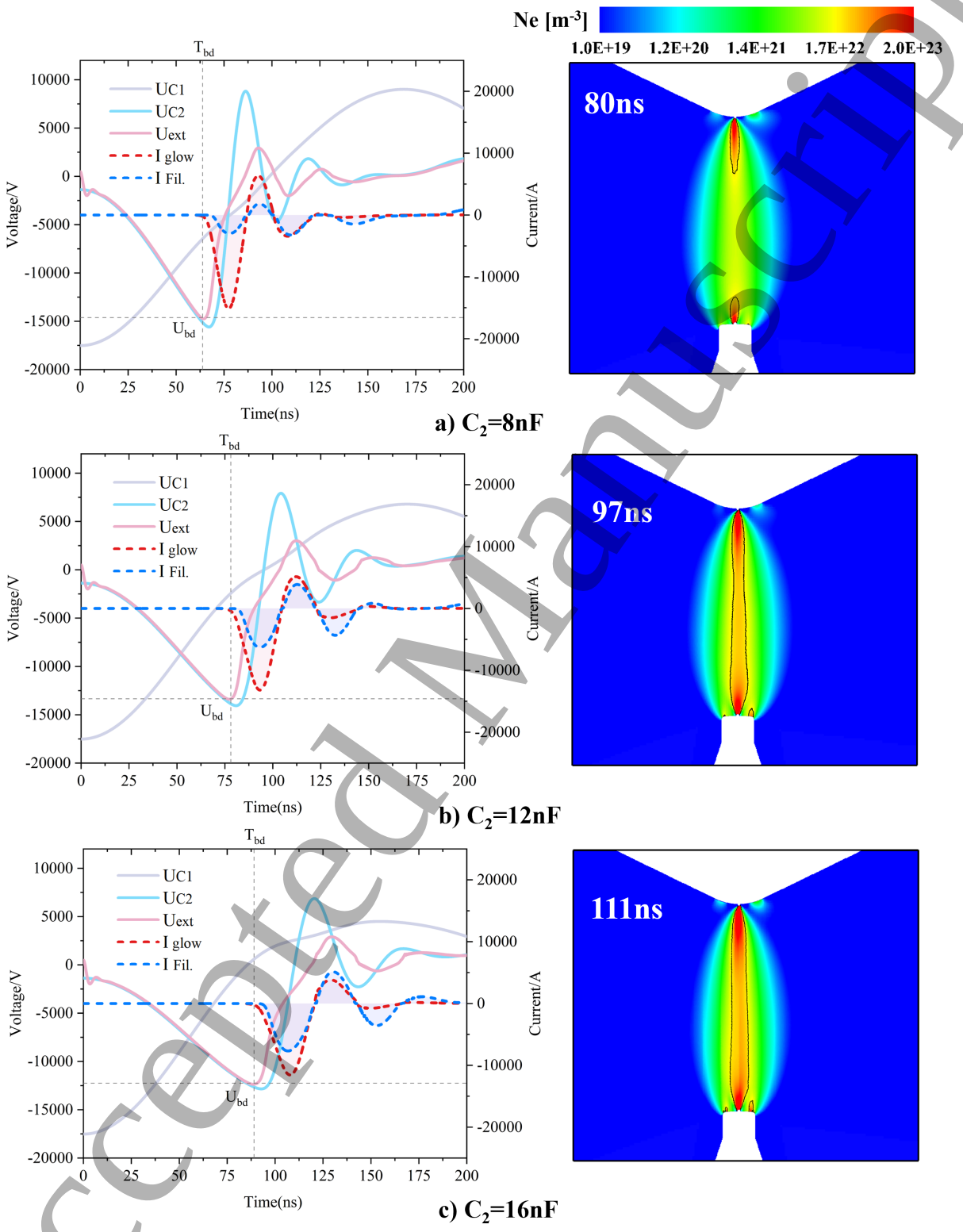

Figure 17: (a-c, left) Temporal evolution of circuit variables under different C_2 values, with T_{bd} (breakdown time), U_{bd} (breakdown voltage), I_{glow} and I_{Fil}. (currents in glow and filament regions), and U_{C1}, U_{C2}, U_{ext} (voltages across capacitors C_1, C_2, and the electrode). (a-c, right) Filament morphology under different C_2 values, with black outlines marking boundaries where electron density exceeds $2 \times 10^{22} m^{-3}$.

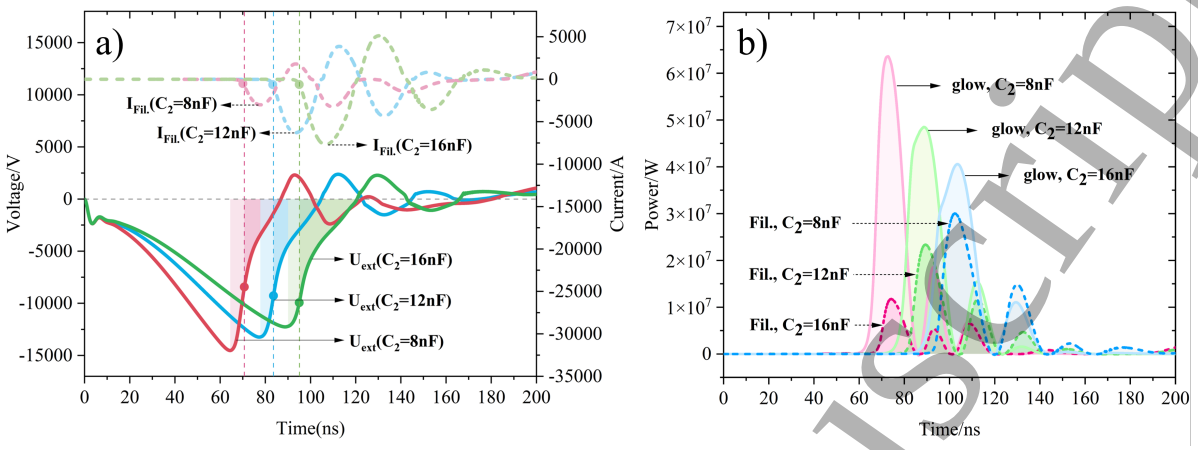

Figure 18: (a) Power evolution of filament and glow discharges under different C_2 values. (b) Electrode voltage distributions during glow–dominated phase (lighter–shaded regions) and filament–dominated phases (darker–shaded regions) for different C_2 values, with lighter–colored dotted and darker–colored solid curves representing filament current and electrode voltage profiles, respectively.

rising edge, shorter pulse duration, and higher peak amplitude, with a lower energy allocation to filamentary discharge. As L_2 increases, the current rise become slower, the peak amplitude decreases, and the energy fraction of filaments gradually rises. Since is directly connected in series with the electrodes, L_2 can be seen as remains in an open–circuit branch before breakdown and only starts to function after breakdown. Therefore, L_2 minimally affects the breakdown timing and voltage. A large L_2 acts as an energy buffer, allowing energy to be injected into the plasma more smoothly, thus providing sufficient time for the highly ionized region near the hotspot to fully develop into filaments.

A smaller L_2 results in a steeper current rise, which leads to a faster voltage drop after breakdown. This is because the electrode voltage $U_{ext} = U_{C2} - L_2 \times dI_p/dt$. A smaller L_2 allows for a higher electrode voltage in the early stage, enabling faster and more intense development of the glow discharge. Subsequently, similar to the mechanism of C_2's influence, the higher current rise rate leads to a rapid voltage drop, causing the voltage to recover to a lower value when filament formation begins. Between the discharge breakdown and peak current, the maximum difference between the electrode voltage and the C_2 voltage can reach 4000–8000 V.

To show this influence process more intuitively, the temporal evolution curves of electrode voltage and filament current for $L_2 = 1$ nH and 6 nH are comparatively plotted in Figure 19(c). By contrasting the electrode voltages, it is observed that at $L_2 = 1$ nH, the voltage remains higher in the early stage and lower in the later stage after breakdown, whereas the $L_2 = 6$ nH case exhibits the opposite trend, with their voltage curves intersecting at a specific time point (Point A). Through the initiation timing of

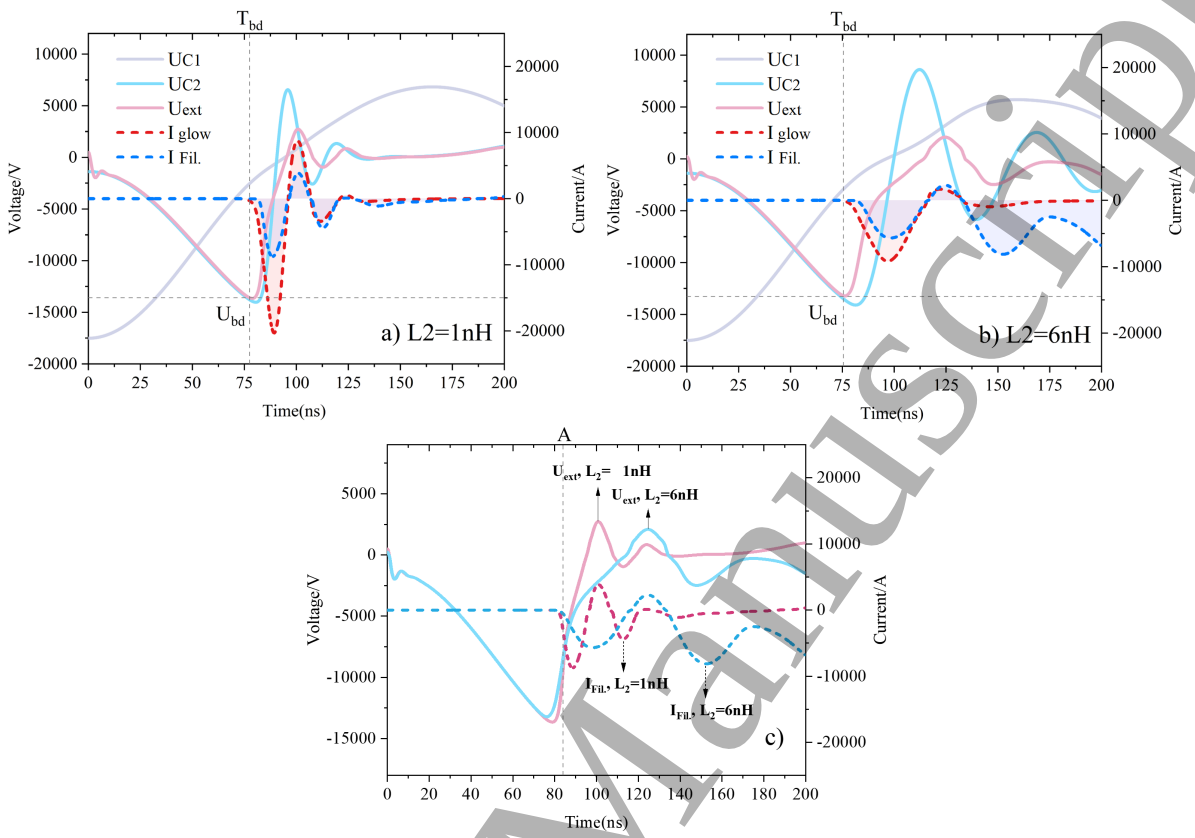

Figure 19: (a-b) Temporal evolution of circuit variables under L_2=1 nH and L_2=6 nH. (c) Comparison of electrode voltage and filament current temporal evolution profiles for L_2=1 nH and L_2=6 nH, where Point A marks the crossover point of the electrode voltage curves between the two cases.

filament current pulses, it is evident that filament development predominantly occurs after the crossover point. The smaller L_2 provides a larger electrode voltage before filament initiation, accelerating the development of glow discharge. Conversely, the low voltage level after filament formation suppresses further filament growth, thereby decreasing the energy fraction allocated to filaments.

As mentioned in Section 3.1, due to severe internal F_2 depletion and a lower ionization threshold in filaments, their intensity still exhibits significant fluctuations during the voltage oscillation phase. In individual cases where filaments develop excessively strong, accompanied by intense halogen depletion, the later–stage voltage oscillations can even induce a 'reverse enhancement' of the filaments. This phenomenon manifests as filaments and their corresponding currents becoming stronger during secondary oscillations than in the initial one. The case with L_2=6nH exemplifies this situation.

In summary, adjusting both L_2 and C_2 can mitigate filaments' "consuming" of glow discharge energy and enhance the overall discharge uniformity. Within the parameter

range discussed in this study, faster energy release correlates with improved uniformity. Notably, adjustments to C_2 exhibit a more pronounced impact on both discharge uniformity and energy allocation between two discharge modes.

4. Conclusions

This study establishes a 0–2D hybrid model focusing on the uniform–filamentary discharge transition in ArF lasers chamber, systematically investigating the dynamic evolution and formation mechanisms of filaments. The simulation shows qualitative agreement with the experimentally observed spatiotemporal evolution of discharge non–uniformity. A semi-quantitative analysis of the impact of filament formation on ArF^* yield is performed, accompanied by recommendations for optimizing discharge uniformity through circuit parameter adjustments. The principal conclusions are summarized as follows:

(1)By introducing micrometre–scale deformations on both the driving and ground electrodes as initial perturbations, the discharges first form high–electron–density plasma regions near the electrode protrusions, accompanied by localized F_2 depletion. This depletion of halogen donors further enhances ionization, creating a positive feedback loop: once initiated by perturbations, the process will self–reinforces, driving the high–density plasma cluster to expand outward along hot spots until it bridges the entire discharge channel, forming a filament approximately 700μm in diameter with high electron density ($>10^{22}m^{-3}$). After filament formation, the dominant electron generation reaction transitions from the collisional ionization of Ar to its stepwise ionization. Concurrently, the primary F_2 consumption reaction transitions from harpoon reaction between Ar^* and F_2, which is also the predominant ArF^* generating reaction during the glow discharge phase, to the dissociative attachment reaction of F_2.

(2)As the volume fraction of filaments increases, the energy deposited in the uniform glow discharge per pulse gradually decreases, and the amplitude of voltage oscillations in the later discharge phase intensifies. Despite occupying a low volumetric proportion ($\leq 2\%$), filaments absorb a substantial fraction (20%–30%) of the input power. However, most of this energy is channeled into ionization processes, resulting in anArF^* production yield per unit energy of only 1/10 to 1/8 of that in the glow discharge region. Under nearly constant total power input, filament formation consequently leads to reductions in both laser power and efficiency. During the filamentation phase, the dominant ArF^* generation pathway shifts from harpoon reactions between Ar and F_2 to three–body recombination reactions involving Ar^+ and F^-. This transition primarily arises from two factors: a) under high ionization degrees, F_2 is extensively consumed via dissociative attachment, generating abundant F^- ions; b) high electron collision frequencies produce a significant population of Ar^+ ions.

(3)Since the complete development of high–density plasma cluster near hotspots into filaments requires 10–15ns, appropriately shortening the power pulse duration can inhibit filament development, reducing discharge non–uniformity. Decreasing the

capacitance of peaking capacitor C_2 or the inductance of discharge stray inductor L_2 can modulate voltage characteristics, promoting the rapid development of initial glow discharge while inhibiting subsequent filament formation and intensification, consequently reducing the energy proportion allocated to filaments. Adjusting C_2 has more pronounced effects on uniformity improvement and filamentation suppression. Within the parameter range considered in this study, faster energy release correlates with enhanced uniformity.

Acknowledegments

The work is supported by the National Natural Science Foundation of China (No.52025064, 52277168, 92271113), National Natural Science Foundation Basic Science Center Project (52488101), National Key Research and Development Program of China (2022YFC2604002). The authors thank the young research group in Atelier des Plasmas for fruitful discussions and the Gongfang Tech Co, Ltd for technical support.

References

[1] C. McAlinden, "Corneal refractive surgery: past to present," *Clinical and Experimental Optometry*, vol. 95, no. 4, pp. 386–398, 2012.

[2] I. Abdelhalim, A. A. Hassan, S. Abdelkawi, S. H. Elnaby, S. Rahbar, and O. Hamdy, "Solid-state laser (266 nm) as an alternative to arf excimer laser (193 nm) for corneal reshaping: Comparative numerical study of the thermal effect," *International Journal for Numerical Methods in Biomedical Engineering*, vol. 40, no. 10, p. e3861, 2024.

[3] K. Kakizaki, Y. Sasaki, T. Inoue, and Y. Sakai, "High-repetition-rate (6khz) and long-pulse-duration (50ns) arf excimer laser for sub-65nm lithography," *Review of Scientific Instruments*, vol. 77, no. 3, 2006.

[4] M. Okoshi, "Fabrication of superhydrophobic silicone rubber with periodic micro/nano-suction cup structure by arf excimer laser-induced photodissociation," *Nanomaterials*, vol. 9, no. 6, p. 870, 2019.

[5] K. Sugioka, T. Akane, K. Obata, K. Toyoda, and K. Midorikawa, "Multiwavelength excitation processing using f2 and krf excimer lasers for precision microfabrication of hard materials," *Applied Surface Science*, vol. 197, pp. 814–821, 2002.

[6] M. Shaheen, J. Gagnon, and B. Fryer, "Experimental studies on ablation characteristics of alumina after irradiation with a 193-nm arf excimer laser," *The European Physical Journal Plus*, vol. 136, no. 1, p. 119, 2021.

[7] S. Amoruso, R. Bruzzese, N. Spinelli, and R. Velotta, "Characterization of laser-ablation plasmas," *Journal of Physics B: Atomic, Molecular and Optical Physics*, vol. 32, p. R131, jul 1999.

[8] A. J. Schmitt and S. P. Obenschain, "The importance of laser wavelength for driving inertial confinement fusion targets. i. basic physics," *Physics of Plasmas*, vol. 30, p. 012701, 2023.

[9] M. Wolford, M. Myers, T. Petrova, J. Giuliani, T. Kessler, M. McGeoch, G. Petrov, A. Schmitt, T. Mehlhorn, and S. Obenschain, "Development of a broad bandwidth 193 nanometer laser driver for inertial confinement fusion," *High Energy Density Physics*, vol. 36, p. 100801, 2020.

[10] M. F. Wolford, M. C. Myers, and T. Petrova, "Final report the physics of high efficiency argon fluoride lasers," tech. rep., 2023.

[11] H. Shields, A. Alcock, and R. Taylor, "Preionization kinetics of an x-ray preionized xecl gas discharge laser," *Applied Physics B*, vol. 31, pp. 27–35, 1983.

[12] T. Hammer and W. Bötticher, "Spectroscopic investigation of the ionization kinetics in xecl laser discharges by xe* density measurements," *Applied Physics B*, vol. 48, no. 1, pp. 73–84, 1989.

[13] A. B. Treshchalov and V. Peet, "Spatial-time dynamics of the discharge pumping and lasing in a xecl excimer laser," *IEEE journal of quantum electronics*, vol. 24, no. 2, pp. 169–176, 1988.

[14] V. M. Borisov, Y. B. Kiryukhin, I. Kochetov, and V. P. Novikov, "Electron kinetics and acoustically induced inhomogeneities of the energydeposited in a pulse-periodic xecl laser," *Soviet Journal of Quantum Electronics*, vol. 15, no. 8, p. 1081, 1985.

[15] R. Arutyunyan, V. Y. Baranov, V. M. Borisov, A. Y. Vinokhodov, and Y. B. Kiryukhin, "Influence of electrode processes on the constriction of a volume dischargein pulse-periodic lasers," *Soviet Journal of Quantum Electronics*, vol. 15, no. 5, p. 639, 1985.

[16] A. B. Treshchalov, A. Lissovski, and E. Chikeev, "High-current discharge pumping of arf, f2 lasers without cathode hot spots and filament instabilities," in *International Conference on Atomic and Molecular Pulsed Lasers IV*, vol. 4747, pp. 253–260, SPIE, 2002.

[17] A. Belasri, J. Boeuf, and L. Pitchford, "Cathode sheath formation in a discharge-sustained xecl laser," *Journal of applied physics*, vol. 74, no. 3, pp. 1553–1567, 1993.

[18] H. Akashi, Y. Sakai, and T. Tagashira, "Modelling of a self-sustained discharge-excited arf excimer laser," *Journal of Physics D: Applied Physics*, vol. 27, no. 6, p. 1097, 1994.

[19] J. Coutts and C. E. Webb, "Stability of transverse self-sustained discharge-excited long-pulse xecl lasers," *Journal of Applied Physics*, vol. 59, pp. 704–710, 1986.

[20] M. J. Kushner, "Microarcs as a termination mechanism of optical pulses in electric-discharge-excited krf excimer lasers," *IEEE transactions on plasma science*, vol. 19, no. 2, pp. 387–399, 1991.

[21] R. Dreiskemper and W. Botticher, "Current filamentation of strongly preionized high pressure glow discharges in ne/xe/hcl mixtures," *IEEE transactions on plasma science*, vol. 23, no. 6, pp. 987–995, 1995.

[22] R. Taylor, "Preionization and discharge stability study of long optical pulse duration uv-preionized xecl lasers," *Applied Physics B*, vol. 41, pp. 1–24, 1986.

[23] N. Belokrinitskii, V. Gorshkov, A. Shchedrin, and D. MILLER, "Effect of inhomogeneities in pre-ionization, electric field, and gas concentration on the arc formation dynamics in self-sustained discharges in xecl lasers," *Technical physics*, vol. 38, no. 5, pp. 409–412, 1993.

[24] A. Demyanov, L. Feenstra, P. Peters, A. Napartovich, and W. Witteman, "Kinetic modelling of a discharge-pumped arf excimer laser and the effects of discharge filamentation," *Applied Physics B*, vol. 72, pp. 823–833, 2001.

[25] U. Krause and J. Kleinschmidt, "One-dimensional model of discharge pumped excimer lasers," *Journal of Applied Physics*, vol. 72, pp. 1237–1243, 1992.

[26] M. Kushner, A. Pindroh, C. Fisher, T. Znotins, and J. Ewing, "Multidimensional modeling of transverse avalanche laser discharges: Applications to the hgbr laser," *Journal of applied physics*, vol. 57, no. 7, pp. 2406–2423, 1985.

[27] Y. I. Bychkov, S. Yampolskaya, and A. Yastremskii, "Two-dimensional simulation of a volume discharge locally inhomogeneous at the cathode in a ne/xe/hcl gas mixture," *Russian Physics Journal*, vol. 55, no. 5, pp. 477–487, 2012.

[28] Y. I. Bychkov, S. Yampolskaya, and A. Yastremsky, "Two-dimensional simulation of initiation and evolution of a plasma channel in the xecl laser pumping discharge," *Laser and Particle Beams*, vol. 21, no. 2, pp. 233–242, 2003.

[29] H. Akashi, Y. Sakai, and H. Tagashira, "Modeling of a micro-streamer initiation and development of arf excimer laser discharges," *Australian journal of physics*, vol. 50, no. 3, pp. 655–669, 1997.

[30] H. Akashi, Y. Sakai, N. Takahashi, and T. Sasaki, "Modelling of the initiation and development of a filamentary discharge in xecl excimer lasers," *Journal of Physics D: Applied Physics*, vol. 32, no. 22, p. 2861, 1999.

[31] Z. Xiong and M. J. Kushner, "Photo-triggering and secondary electron produced ionization in electric discharge arf* excimer lasers," *Journal of Applied Physics*, vol. 110, p. 083304, 2011.

[32] C. Li, W. Brok, U. Ebert, and J. Van der Mullen, "Deviations from the local field approximation in negative streamer heads," *Journal of applied physics*, vol. 101, no. 12, 2007.

[33] G. Grubert, M. Becker, and D. Loffhagen, "Why the local-mean-energy approximation should be used in hydrodynamic plasma descriptions instead of the local-field approximation," *Physical Review E*, vol. 80, no. 3, p. 036405, 2009.

[34] Y. Zhu, S. Shcherbanev, B. Baron, and S. Starikovskaia, "Nanosecond surface dielectric barrier discharge in atmospheric pressure air: I. measurements and 2d modeling of morphology, propagation and hydrodynamic perturbations," *Plasma Sources Science and Technology*, vol. 26, no. 12, p. 125004, 2017.

[35] Y. Zhu, X. Chen, Y. Wu, J. Hao, X. Ma, P. Lu, and P. Tardiveau, "Simulation of ionization-wave discharges: a direct comparison between the fluid model and e-fish measurements," *Plasma Sources Science and Technology*, vol. 30, no. 7, p. 075025, 2021.

[36] G. Hagelaar and L. C. Pitchford, "Solving the boltzmann equation to obtain electron transport coefficients and rate coefficients for fluid models," *Plasma sources science and technology*, vol. 14, no. 4, p. 722, 2005.

[37] P. Almeida, M. Benilov, and G. Naidis, "Calculation of ion mobilities by means of the two-temperature displaced-distribution theory," *Journal of Physics D: Applied Physics*, vol. 35, no. 13, p. 1577, 2002.

[38] C. S. Peskin, "The immersed boundary method," *Acta numerica*, vol. 11, pp. 479–517, 2002.

[39] X. Ma, L. Bai, Y. Zhu, X. Jiang, and Y. Wu, "Numerical investigation of discharge evolution and breakdown characteristics of arf excimer lasers," *Plasma Sources Science and Technology*, vol. 33, p. 075012, 2024.

[40] S. Pancheshnyi, *Experimental study, direct nimerical simulation and application of ionization wave.* PhD thesis, 01 2007.

[41] R. Dreiskemper, G. Schroder, and W. Botticher, "Light emission during cathode sheath formation in preionized high-pressure glow discharges," *IEEE Transactions on Plasma Science*, vol. 23, pp. 180–187, 1995.

[42] R. Dreiskemper, *Kathodenbedingte Instabilitäten transienter Hochdruckglimmentladungen: eine experimenteller Beitrag.* PhD thesis, Verlag nicht ermittelbar, 1993.

[43] X. Guo, J. Ding, Y. Zhou, and Y. Wang, "Corrosion behaviors of the copper alloy electrodes in arf excimer laser operation process," *High Power Laser Science and Engineering*, vol. 6, p. e9, 2018.